Journal Pre-proof

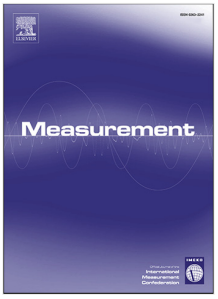

Identification of liquid-vapor phase transition using the co-occurrence matrix and Haralick features

Ana Oprisan, Sorinel A. Oprisan, Yves Garrabos,
Carole Lecoutre-Chabot, Daniel Beysens

PII: S0263-2241(25)01875-5
DOI: https://doi.org/10.1016/j.measurement.2025.118516
Reference: MEASUR 118516

To appear in: *Measurement*

Received date : 7 December 2024
Revised date : 8 July 2025
Accepted date : 22 July 2025

Please cite this article as: A. Oprisan, S.A. Oprisan, Y. Garrabos et al., Identification of liquid-vapor phase transition using the co-occurrence matrix and Haralick features, *Measurement* (2025), doi: https://doi.org/10.1016/j.measurement.2025.118516.

Highlights (for review, without author details)

Highlights

- Gas-liquid phase transitions can be identified from recorded light-transmitted fluctuations
- Second-order image statistics distinguishes between fluctuations and phase separation
- Energy, Contrast, and Correlation features identifying a gas-liquid phase transition
- Haralick features scale with bit depth and displacement vector

Identification of Liquid-Vapor Phase Transition using the Co-occurrence Matrix and Haralick Features

Abstract

Identification of a phase transition—specifically, the precise timing of the critical temperature crossing—is challenging due to the thermal inertia of the enclosure holding the fluid, the fluid's finite thermal conductivity, convective flows, and sedimentation. The human eye is particularly well adapted to detecting such phase transitions in images produced by transmitted light through critical fluids. In this study, we used Haralick image features that most closely correspond to human visual perception to identify gas–liquid phase transitions. The images were recorded during the phase transition of sulfur hexafluoride (SF_6) in microgravity—a particularly challenging scenario.

The first goal of this study was to demonstrate that Haralick features can identify a phase transition from recorded images of supercritical fluids in microgravity. While highly sensitive to minute changes in image detail, Haralick features are not inherently normalized; thus, conclusions based on their values for a given image bit depth cannot be reliably compared to those derived from images captured with different cameras or quantization schemes.

The second goal of this study was to identify empirical scaling laws for Haralick features that enable the prediction of their behavior as image bit depth varies. Such flexibility would allow direct comparison of results obtained from phase transition datasets recorded using different quantization schemes and imaging systems.

Keywords: Supercritical Fluids, Microgravity, Fluctuations, Phase Separation, Image Processing, Scaling Laws, Haralick Features

1. Introduction

Since their introduction over five decades ago, Haralick features [1, 2] have become some of the most widely used tools in image analysis and

classification [3]. The human visual system is particularly adept at perceiving image characteristics such as "smoothness" and "granularity," which are governed by second-order statistics to which the brain is naturally attuned [4]. In grayscale images, first-order statistics capture intensity-based moments—such as the mean and variance—derived from the image histogram. An image $I(x, y)$ is defined as a two-dimensional array of size $N_x \times N_y$, where each coordinate (x, y) represents the light intensity at a specific pixel. For grayscale images, these intensity values $I(x, y)$ are integers within the range $N_g = 0$ to $2^b - 1$, known as gray levels, where b is the image's bit depth. For example, a binary black-and-white image has $b = 1$ and two gray levels: 0 (black) and 1 (white). In this study, we use grayscale images with $b = 8$, i.e., $N_g = 256$ levels ranging from 0 (black) to 255 (white). Second-order statistics rely on a bivariate histogram that captures the co-occurrence of intensity values at neighboring pixel locations—a process believed to be mimicked by the human visual cortex [5].

The Gray Level Co-occurrence Matrix (GLCM), denoted $P_d(i, j)$, is a bivariate histogram that counts how often pixel intensities i and j occur at a specific distance $d = (\Delta x, \Delta y)$ (in pixels) from each other. The GLCM is a square matrix of size $N_g \times N_g$, where N_g is the number of gray levels in the image. Haralick proposed a set of scalar, dimensionless features derived from the GLCM to summarize texture patterns [1, 2]. In this work, we use three commonly cited Haralick features—Energy f_1 (Eq. 3), Contrast f_2 (Eq. 4), and Correlation f_3 (Eq. 6)—to analyze critical fluids [6, 7]. One reason for the widespread adoption of Haralick features is their robustness to image noise, which has minimal impact on texture analysis performance [8].

The macroscopic mechanical properties of materials are deeply influenced by their microstructure, which evolves in response to mechanical, thermal, or operational stresses. Phase separation plays a key role in materials processing, including in metallic alloys [9], polymer blends, and polymer–liquid crystal mixtures [10]. Analyzing microstructural features helps elucidate the bulk properties of materials. The GLCM and Haralick features have proven highly sensitive to phase transitions and are effective for quantifying thermophysical properties across diverse applications. Examples include identifying metallurgical phases in steel microstructures [11], tracking surface hardening during steel cooling [12], detecting two-phase transitions in steel [13], and analyzing changes in microstructure due to tempering parameters [14].

In soft condensed matter systems, Haralick features have been employed to detect phase transitions in polymers and liquid crystals (see [15, 16] and

references therein). They have also enabled quantitative estimation of thermophysical properties, including shear modulus, failure temperature, and zero-shear viscosity in polymeric colloids [17].

As a fluid approaches its critical point, thermal fluctuations induce small variations in local density, which in turn cause minute changes in the refractive index [10, 18, 19, 20, 21]. These density fluctuations disrupt the transmitted light intensity [18, 19, 22, 23, 24, 25, 26]. Near the critical point, the fluctuations become long-ranged [27] and follow universal power-law behaviors that govern physical quantities such as thermal compressibility and correlation length [28].

Gas–liquid mixtures near the critical temperature T_c have been widely studied [29, 30, 31, 32, 33, 34, 35, 36, 37, 38, 39, 40, 41, 42, 43, 44, 45, 46]. Due to the high compressibility near T_c, such experiments are often conducted in microgravity to avoid gravitational sedimentation and to suppress convective flows [24, 31, 47, 48, 49].

When a control parameter (e.g., temperature) shifts and initiates phase separation, minority domains grow dynamically in an out-of-equilibrium process. Phase separation is not only a model system for non-equilibrium statistical physics [50], but also holds significant practical importance [51, 52, 53]. Two-phase heat and mass transfer processes [54, 55] are fundamental to a wide range of engineering applications [56, 57, 58].

Despite the effectiveness of Haralick features in texture classification, careful consideration must be given to the GLCM parameters used in their computation. For example, the image quantization scheme defines the number of gray levels N_g, and thus the size of the GLCM. Reducing bit depth enables faster computation but may lead to the loss of critical image information. Moreover, Haralick features are sensitive to the choice of displacement vector $d = (\Delta x, \Delta y)$ (in pixels). Yet, this dependency is typically explored only qualitatively or empirically. Because Haralick features are not normalized, variations in bit depth or displacement vector can produce vastly different values for the same image. Ideally, one would derive analytical models that predict how Haralick features scale with N_g and d—improving reproducibility and enabling diagnostic standardization [59].

In the absence of such models, this study aims to: (1) *evaluate whether the three most commonly used Haralick features—Energy f_1, Contrast f_2, and Correlation f_3—are qualitatively sensitive to phase transitions in supercritical fluids*; and (2) *empirically determine scaling laws for these features that could be generalized to other critical phenomena and refined over time.*

Although Haralick features have been extensively used in image analysis, to our knowledge, no prior study has applied them to characterize phase transitions in supercritical fluids. While a complete theoretical framework linking light transmission and image formation in critical fluids is still emerging, this work leverages the well-documented SF_6 phase transition in microgravity—an especially challenging environment [43, 60, 61]—to qualitatively and quantitatively relate Haralick features to the macroscopic structures observed in the resulting images.

The manuscript is organized as follows. Section 2.1 describes the experimental data obtained under microgravity conditions. Section 2.2 reviews the GLCM and the three Haralick features used: Energy f_1, Contrast f_2, and Correlation f_3. The results begin in Section 3.1 with an analysis of Energy f_1, demonstrating its sensitivity to morphological changes during phase transitions. We derive an empirical scaling law, $f_1 \propto {N_g}^{\alpha_1} d^{\beta_1}$, where α_1 and β_1 are scaling exponents for N_g and the displacement vector magnitude d, respectively. We observe similar sensitivity for Contrast f_2 (Section 3.2) and Correlation f_3 (Section 3.3). Section 4 offers a concise discussion contextualized within related literature.

2. Materials and Methods

2.1. Transmitted Light Through a Supercritical Fluid in Microgravity

The ALICE2 facility [29, 62] was used to record images of density fluctuations near the critical point of the pure fluid SF_6 under microgravity conditions. Details of the experimental setup can be found in [29, 38, 43, 61, 63, 64, 65, 66, 67]. SF_6 is among the most convenient working fluids used in weightlessness to investigate critical-point phenomena. Indeed, SF_6 is an inert gas with a moderate critical pressure of $p_c \approx 3.8\,\mathrm{MPa}$, a critical temperature of $T_c \approx 45.6\,^{\circ}\mathrm{C}$ ($T_c \approx 318.733\,\mathrm{K}$), and a critical density of $\rho_c \approx 734.3\,\mathrm{kg/m^3}$, which facilitate experimentation [64, 68, 69]. Notably, it was the working fluid in the ALICE2 experiments conducted aboard the MIR space station between 1996 and 1999, which produced a wealth of images near the critical point.

A cylindrical sample cell with an inner diameter of 12 mm and an inner thickness of 3.023 mm was filled with 99.98 % pure electronic-grade SF_6 (Alpha Gaz–Air Liquide) at a mean density slightly above the critical value [64]. Specifically, the fluid was prepared with a reduced density $\rho^* = (\rho - \rho_c)/\rho_c = \pm\, 0.02\,\%$, where ρ is the mean density and ρ_c is the critical density [64].

Light intensity measurements were performed using a He–Ne laser with a vacuum wavelength $\lambda_0 = 632.8\,\mathrm{nm}$, a maximum power of approximately 1 mW, and a laser stability better than 0.3 % after one hour [64]. Initially, the sample cell was maintained at a constant temperature above T_c for about 40 min (denoted the UP region in Fig. 1a). Subsequently, a thermal quench of 300 µK lowered the temperature below T_c, where it was held for another 40 min (the DOWN region in Fig. 1a). The onset of fluid separation following the quench confirms that T_c lies between the UP and DOWN plateaux shown in Fig. 1a [43, 60]. The temperature shown in Fig. 1a was recorded by a thermistor embedded in the copper wall of the sample cell, providing an approximation of the actual fluid temperature. This reading is influenced by the higher thermal conductivity of the wall compared to that of the fluid bulk [43, 61]. The temperature change during the quench occurred over approximately 10 s, as indicated in Fig. 1.

Images were recorded at 25 frames per second. Each frame was an 8-bit grayscale image with dimensions 176×240 pixels and a spatial resolution of 3 µm per pixel. This study focuses on the phenomena observed during the early stages of phase separation.

Two types of light-scattering images were captured during the experiment: (i) *microscopic view* images, acquired through a microscope objective and analyzed in this study (see Fig. 1b and Fig. 1c); and (ii) *full view* images, recorded without the microscope.

In the UP region, the first half of the microscopic images were focused on the exit window of the sample cell, while the second half (including all DOWN region images) was focused on the cell's mid-plane. We analyzed 160 microscopic images from the UP region (approximately 6.4 s of recording) and 489 microscopic images from the DOWN region (approximately 19.5 s), as illustrated in Fig. 1a. Between these two recording periods, 472 full-view images (approximately 18.9 s) were captured without the microscope and were excluded from the analysis.

Previous estimates of T_c using the histogram method placed it about 47 µK above the DOWN plateau [43]. Using the dynamic structure factor method, T_c was estimated to lie between 15 µK to 42 µK above the DOWN plateau for the same dataset [61, 70].

As shown in Fig. 1b, the density fluctuations observed above T_c appear structureless. However, immediately below T_c, interconnected domains begin to form, serving as precursors to phase separation—clearly visible in Fig. 1c.

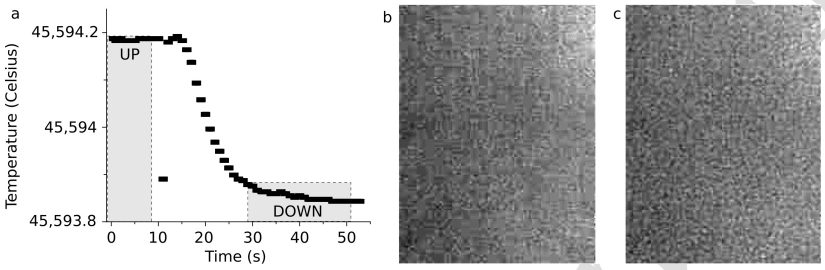

Figure 1: **Critical Fluctuations Above and Below Critical Temperature.** (a) Temperature profile during the final 300 µK thermal quench crossing T_c. The first shaded region marks the acquisition of 160 images in the UP region ($T > T_c$), spanning approximately 6.4 s. The second shaded region marks the 489 images recorded in the DOWN region ($T < T_c$), spanning approximately 19.5 s [61]. (b) A representative image from the middle of the UP region.
(c) A representative image from the middle of the DOWN region.

2.2. Gray Level Co-occurrence Matrix (GLCM)

The light intensity $I(x, y)$ in a two-dimensional grayscale image of size $N_x \times N_y$ is quantized and stored as an array of integers ranging over N_g gray levels. In this study, we employed the default image intensity quantization scheme, in which $I(x, y)$ takes N_g evenly spaced discrete values ranging from 0 (black pixels) to $N_g - 1$ (white pixels). The number of intensity bins N_g is related to the image bit depth b through $N_g = 2^b$. A Cartesian coordinate system with the origin at the upper-left corner of the image is used, as shown in Fig. 2a. The displacement (or offset) vector $d = (\Delta x, \Delta y)$ defines a horizontal shift Δx (rightward) and a vertical shift Δy (downward), both measured in pixel units, between a reference (starting) pixel and its corresponding target (neighboring) pixel.

The example in Fig. 2b shows a quantized image of size $N_x = 5$ and $N_y = 3$, with a bit depth of $b = 2$, resulting in $N_g = 2^b = 4$ gray levels, i.e., $N_g = \{0, 1, 2, 3\}$.

The GLCM counts how many times a reference pixel with gray level i co-occurs with a neighbor of gray level j at a displacement $d = (\Delta x, \Delta y)$ pixels from each other [1]:

$$P_d(i, j) = \#\{((x_i, y_i), (x_j, y_j)) : I(x_i, y_i) = i \;\&\; I(x_j, y_j) = j\}, \tag{1}$$

where # denotes the count of such pixel pairs. Here, (x_i, y_i) are the coordinates of the reference pixel with intensity i, and $(x_j, y_j) = (x_i + \Delta x, y_i + \Delta y)$

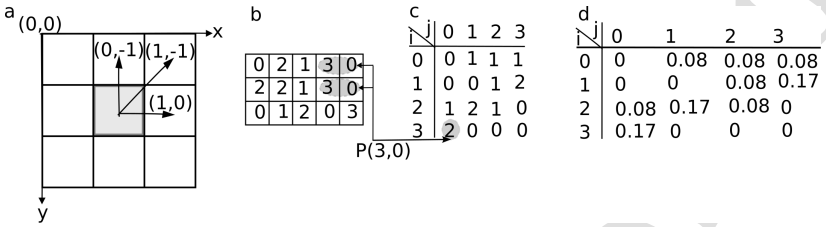

Figure 2: **Gray Level Co-occurrence Matrix (GLCM).** (**a**) Neighboring pixels relative to a central (reference) pixel (shaded) are identified by the displacement vector $d = (\Delta x, \Delta y)$ (in pixels). For instance, the first-order neighbor up and to the right corresponds to $d = (1, -1)$ pixels. (**b**) A 5×3 image with 2-bit quantization. For $d = (1, 0)$ pixels, the two elliptical shaded areas mark the only pixel pairs with gray levels $i = 3$ and $j = 0$. (**c**) The resulting GLCM $P_d(i, j)$ for the image in (b) with $d = (1, 0)$ pixels. The entry $P_d(3, 0) = 2$ reflects the two shaded pairs. (**d**) The corresponding normalized GLCM $p_d(i, j)$.

are those of the neighboring pixel with intensity j. For instance, in Fig. 2b, with $d = (1, 0)$ pixels, two pixel pairs have $(i = 3, j = 0)$, resulting in $P_d(3, 0) = 2$ in Fig. 2c.

The normalized GLCM is defined as:

$$p_d(i, j) = \frac{P_d(i, j)}{\sum_{i=0}^{N_g-1} \sum_{j=0}^{N_g-1} P_d(i, j)}. \tag{2}$$

In an image of size $N_x \times N_y$, the number of horizontal pixel pairs for $d = (1, 0)$ pixels is $R_x = (N_x - 1)N_y$, and for vertical displacement $d = (0, 1)$ pixels, it is $R_y = (N_y - 1)N_x$. In the example from Fig. 2b, $R_x = 12$ and $R_y = 10$. The normalized GLCM shown in Fig. 2d for a displacement vector of $d = (1, 0)$ pixels satisfies $p_d(3, 0) = P_d(3, 0)/R_x = 2/12 \approx 0.17$.

Note that the GLCM in Fig. 2c is asymmetric. However, Haralick's original definition [1, 2] uses a symmetric version that counts both $i \to j$ and $j \to i$ transitions (e.g., $3 \to 0$ and $0 \to 3$).

From this point onward, we adopt the symmetric GLCM definition and drop the subscript d for notational simplicity.

Angular Second Moment (ASM), or Energy, measures image ho-

mogeneity and is defined as [1, 2]:

$$f_1 = \sum_{i=0}^{N_g-1} \sum_{j=0}^{N_g-1} p(i,j)^2. \tag{3}$$

Higher ASM values indicate greater homogeneity. For a completely uniform image with a single gray level (e.g., $i = 0$), $p(0,0) = 1$ and all other entries are zero, yielding the maximum energy $f_1 = N_g^2$.

Contrast (CON) quantifies the intensity difference between neighboring pixels and is defined as [1, 2]:

$$f_2 = \sum_{k=0}^{N_g-1} k^2 \, p_{x-y}(k), \tag{4}$$

where the marginal distribution $p_{x-y}(k)$ is:

$$p_{x-y}(k) = \sum_{i=0}^{N_g-1} \sum_{j=0}^{N_g-1} \delta_{|i-j|,k} \, p(i,j), \tag{5}$$

with $\delta_{m,n}$ denoting the Kronecker delta.

The function $p_{x-y}(k)$ aggregates GLCM entries where the absolute intensity difference between pixel pairs is k. For example, $p_{x-y}(0)$ sums entries along the GLCM's main diagonal, while $p_{x-y}(1)$ sums the first diagonals above and below it. Lower contrast values correspond to minimal intensity differences, while larger differences contribute more heavily due to the k^2 weighting. For a purely diagonal GLCM, where $i = j$, the contrast is $f_2 = 0$.

Correlation (COR) captures the linear dependency between the gray levels of neighboring pixels and is defined as [1, 2]:

$$f_3 = \frac{\sum_{i=0}^{N_g-1} \sum_{j=0}^{N_g-1} ij \, p(i,j) - \mu_x \mu_y}{\sigma_x \sigma_y}, \tag{6}$$

where

$$p_x(i) = \sum_{j=0}^{N_g-1} p(i,j), \quad p_y(j) = \sum_{i=0}^{N_g-1} p(i,j) \tag{7}$$

are the marginal distributions of the reference and target pixel gray levels. Since the GLCM is symmetric, $p_y = p_x^T$.

The distribution $p_x(i)$ represents the probability of observing gray level i at a distance $|d|$ from any other pixel—essentially, the likelihood of gray level i occurring within a circular neighborhood of radius $|d|$. The mean and standard deviation are defined as:

$$\mu_x = \sum_{i=0}^{N_g-1} i\, p_x(i), \quad \sigma_x^2 = \sum_{i=0}^{N_g-1} (i-\mu_x)^2\, p_x(i). \tag{8}$$

The correlation f_3 ranges between 0 and 1. A value of $f_3 = 0$ indicates no spatial correlation. For example, if all gray levels are equally likely at any displacement, the image is purely noisy and the GLCM becomes uniform: $p(i,j) = 1/N_g^2$. This implies $p_x(i) = 1/N_g$, $\mu_x = \mu_y = (N_g-1)/2$, and the double summation in Eq. 6 becomes:

$$\sum_{i=0}^{N_g-1}\sum_{j=0}^{N_g-1} \frac{ij}{N_g^2} = \left(\frac{1}{N_g}\sum_{i=0}^{N_g-1} i\right)^2 = \left(\frac{N_g-1}{2}\right)^2,$$

which exactly cancels the numerator of Eq. 6, yielding $f_3 = 0$, confirming the absence of correlation.

3. Results

In the following, we present all results obtained above the critical temperature T_c (UP dataset) using red circles, and those below T_c (DOWN dataset) using blue stars.

3.1. Energy Feature f_1

The Angular Second Moment (ASM), also known as the Energy feature, quantifies image homogeneity [1]. It is computed as the sum of the squares of all normalized GLCM entries, as defined in Eq. 3. The value of f_1 lies in the range $[0, 1]$, with 1 corresponding to a perfectly homogeneous image. Such images contain only a few dominant gray-tone transitions, resulting in a GLCM $P_d(i,j)$ with a small number of large entries and many near-zero ones. Therefore, f_1 is primarily influenced by these high-magnitude entries in homogeneous textures, leading to large values.

As shown in Fig. 3a, f_1 values above T_c (red circles) are consistently higher than those below T_c (blue stars). The mean $\pm$ standard deviation of f_1 is 0.037 ± 0.015 for the UP dataset and 0.017 ± 0.003 for the DOWN

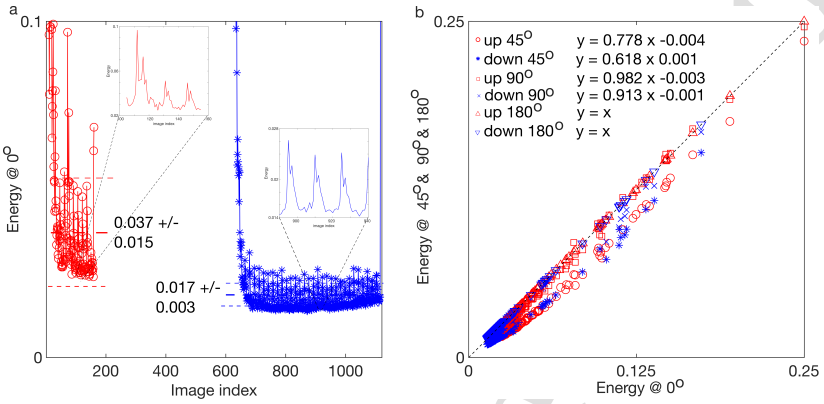

Figure 3: **Energy feature f_1 for 8-bit images and horizontal displacement of $d = (1, 0)$ pixels.** (a) f_1 values above T_c (red circles) are higher than those below T_c (blue stars), reflecting stronger light scattering and longer-range correlations. Immediately below T_c, the images become more homogeneous, lowering f_1. Thick dashed lines indicate mean values; thin dashed lines denote one standard deviation. Insets show periodic fluctuations in f_1 over 50 frames, with a dominant frequency of approximately 1.7 Hz. Initial high values in the DOWN region likely reflect microscope movement. (b) f_1 values for different displacement vector orientations, plotted against the horizontal displacement baseline. The slopes from linear fits indicate anisotropy in spatial structure.

dataset, indicating a statistically significant difference. This suggests that f_1 is sensitive to the strong image fluctuations caused by light scattering above T_c. Below T_c, as phase separation sets in, the scattering diminishes and the images appear more uniform, reducing f_1.

The variation in f_1 across time is substantial and stable, as illustrated in the insets of Fig. 3a. The coefficient of variation (CV) is relatively high: 0.40 for the UP dataset and 0.18 for the DOWN dataset. This may partly result from differences in microscope focus: the first half of the UP images was acquired with focus on the cell's exit window, whereas the second half—including all DOWN images—was focused on the cell's mid-plane. This is evident in Fig. 3a, where greater variability is observed in the first half of the UP dataset. Additionally, both datasets exhibit intrinsic variability, evident from persistent oscillations in f_1 with a dominant frequency near 1.7 Hz (15 frames at 25 fps), likely due to mechanical vibrations (see [71] for MIR/ISS vibration analysis).

We also investigated how f_1 depends on the orientation of the displace-

ment vector. In Fig. 3b, results for a horizontal displacement of $d = (1, 0)$ pixels are compared with those at 45° ($d = (1, 1)$ pixels), 90° ($d = (0, -1)$ pixels), and 180° ($d = (-1, 0)$ pixels). Rather than presenting raw f_1 values, we compare each orientation's f_1 to the horizontal reference. If the values matched, points would lie on the diagonal (dashed line). Only the 180° (leftward) orientation lies on the diagonal, indicating horizontal symmetry. For 90°, values are slightly lower (slope ≈ 0.9), suggesting mild anisotropy, possibly due to residual gravity or weak temperature gradients aboard the MIR station.

Diagonal orientations (e.g., 45°) show even lower f_1 values, with correlation slopes between 0.618 and 0.778. This is unlikely to reflect true directional homogeneity and is more plausibly attributed to vector magnitude. Horizontal and vertical displacements have a magnitude of $|d| = 1$ pixel, while diagonal displacements have $|d| = \sqrt{2} \approx 1.414$ pixels. This suggests a potential inverse relationship:

$$f_1 \propto \frac{1}{|d|}. \tag{9}$$

The asymptotic behavior of Haralick features with the magnitude $|d|$ of the displacement vector, as shown in Eq. 9, implies a scale-invariant or fractal-like structure and long-range correlation in the image textures, where correlation strength decreases predictably with distance. At small d, neighboring pixels tend to have very similar gray levels in most natural or slowly varying textures. This means that one or two entries of the GLCM dominate; thus, f_1 is relatively large. As d increases, more distant pixels are sampled, leading to greater gray-level mixing and more off-diagonal $p(i, j)$ entries. As a result, the Energy feature, computed from a more uniform GLCM, yields a lower f_1 value. A power-law dependence of any Haralick feature proportional to $d^{-\beta}$ implies that doubling the distance between pixel pairs causes the Haralick feature to decrease by a factor of 2^{β}.

Another factor influencing f_1 is image bit depth. Bit depth may vary due to filtering, noise reduction, or acquisition settings. To assess its impact, we computed f_1 on the same image set across different bit depths (quantization schemes). As shown in Fig. 4, lower bit depths consistently lead to higher f_1 values.

This trend arises because reducing bit depth decreases the number of GLCM bins while preserving the number of pixel pairs. Consequently, the GLCM has fewer but larger entries, increasing f_1.

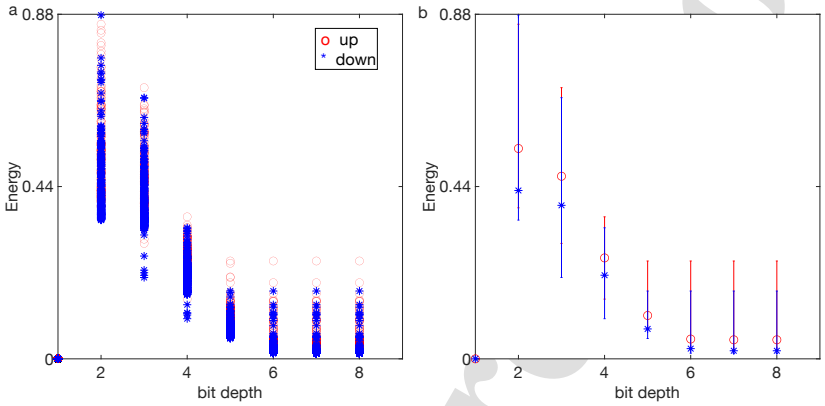

Figure 4: **Effect of bit depth on Energy feature f_1.** (a) f_1 values above T_c (red circles) and below T_c (blue stars). (b) Mean and standard deviation of f_1 show a decreasing trend with increasing bit depth.

a

0	2	1	3	0
2	2	1	3	0
0	1	2	0	3

b

0	1	0	1	0
1	1	0	1	0
0	0	1	0	1

c

i \ j	0	1	2	3
0	0	1	1	1
1	0	0	1	2
2	1	2	1	0
3	2	0	0	0

d

i \ j	0	1
0	1	5
1	5	1

Figure 5: **Bit depth reduction and its effect on f_1.** (a) A 3×5 image at 2-bit depth ($N_g = 4$). (b) The same image at 1-bit depth ($N_g = 2$). (c) The corresponding 4×4 GLCM (2-bit image). (d) The 2×2 GLCM (1-bit image).

In Fig. 5c, the 2-bit GLCM includes many small values: $f_1 = 6(1/12)^2 + 3(2/12)^2 = 0.125$. The 1-bit GLCM in Fig. 5d has fewer but larger values: $f_1 = 2(1/12)^2 + 2(5/12)^2 = 0.361$. This results from dropping the least significant bit and combining gray levels (e.g., 0 and 1 $\rightarrow$ 0; 2 and 3 $\rightarrow$ 1) [7].

Figure 4 suggests that f_1 does not scale linearly with N_g. Histograms of f_1 across bit depths (Fig. 6) confirm this. For example, in Fig. 6a3 (8-bit UP data), most f_1 values exceed 0.016, while in Fig. 6b3 (8-bit DOWN), they fall below it. Furthermore, histograms for 8-bit, 4-bit, and 2-bit data show minimal overlap. The approximate ranges are:

- 8-bit: $[0.01, 0.1]$
- 4-bit: $[0.16, 0.35]$
- 2-bit: $[0.35, 0.88]$

These results support an empirical relationship:

$$f_1 \propto \frac{1}{N_g}. \tag{10}$$

The scaling law given by Eq. 10 enables direct comparison of Haralick features across non-homogeneous datasets obtained using different quantization schemes.

Figure 6 also shows that the f_1 distribution in the UP dataset (a1–a3) is consistently broader than in the DOWN dataset (b1–b3). This is expected, as light scattering near and above T_c is more intense and leads to greater pixel variability. Universal amplitude ratios from critical phenomena suggest that fluctuation amplitudes and correlation lengths are roughly twice as large above T_c as below [46]. Below T_c, domain growth begins, enhancing light scattering contrast (see further analysis below).

3.2. Contrast Feature f_2

As defined by Haralick, "the contrast feature f_2 is a difference moment of the GLCM and is a measure of the contrast or the amount of local variations present in an image" [1]. The f_2 feature emphasizes local dissimilarities by assigning higher weights to GLCM entries with large differences in gray levels and lower weights to entries with similar gray levels. In contrast, the f_1 (Energy) feature weights all GLCM entries equally and is thus more sensitive

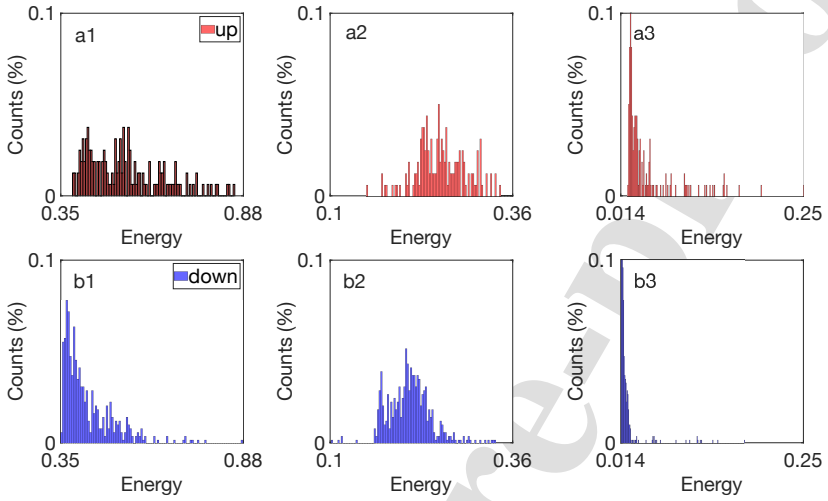

Figure 6: **Histograms of Energy feature f_1.** Panels a1–a3: UP dataset at 2-bit, 4-bit, and 8-bit depths. Panels b1–b3: DOWN dataset at matching bit depths. Bit depth strongly influences the f_1 range and distribution, with minimal overlap between depths.

to overall image homogeneity—for instance, during the uniform phase just below T_c in early-stage phase separation.

The f_2 feature is particularly effective at highlighting local intensity variations, such as the edges between liquid and vapor domains seen in Fig. 1c. This contrasts with the low f_2 values associated with more uniform textures, like the image shown in Fig. 1b. Quantitatively, this distinction is reflected in the increased f_2 values observed during the onset of phase separation, as illustrated in Fig. 7a.

Interestingly, the lower f_2 values observed above T_c suggest that the GLCM entries are concentrated near the principal diagonal (where $|i - j| = 0$), implying that pixel intensities are spatially correlated and not randomly distributed.

Image contrast in this context is governed by local refractive index gradients, which are, in turn, determined by local density gradients. Above T_c, these density gradients arise from thermal fluctuations and are modulated by the thermodynamic coupling parameter $\left(\frac{\partial \rho}{\partial T}\right)_p$, which diverges at T_c and allows these fluctuations to become optically observable. The characteristic

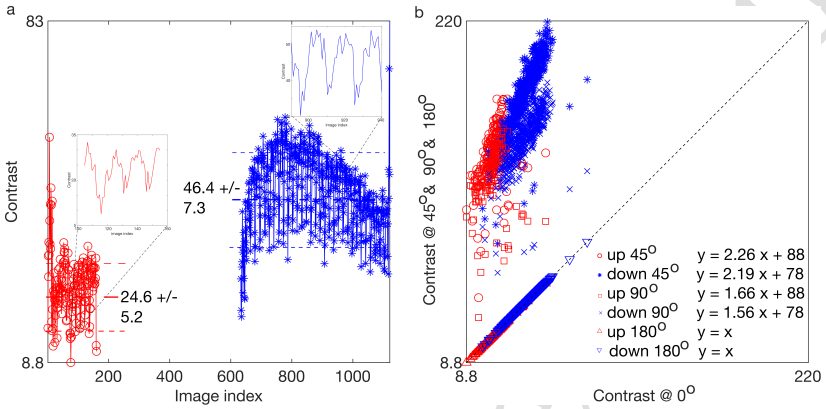

Figure 7: **Contrast feature f_2 for 8-bit depth images with a horizontal displacement vector of $d = (1, 0)$ pixels.** (a) Below T_c (red circles), f_2 values are statistically higher than those above T_c (blue stars). Insets show periodic oscillations across intervals of 15 images. The elevated f_2 values above T_c are consistent with universal amplitude ratios in critical phenomena, where the amplitude and range of density fluctuations are approximately twice as large above T_c compared to below [46]. (b) f_2 values for different displacement orientations plotted against the horizontal baseline. Slopes indicate directional variation in contrast.

length scale for these gradients is the correlation length ξ. Below T_c, contrast is further enhanced by the formation of liquid–vapor domains, where sharp interfaces—also on the order of ξ—produce larger refractive index gradients. Although the system is in a quasi-stationary state below T_c, these domains continue to grow, originating from fluctuations of size ξ seeded at the moment of the thermal quench.

In addition to the horizontal displacement vector of $d = (1, 0)$ pixels analyzed in Fig. 7a, panel (b) presents f_2 values for orientations at 45° ($d = (1, 1)$ pixels), 90° ($d = (0, -1)$ pixels), and 180° ($d = (-1, 0)$ pixels). The near-identical f_2 values for rightward (0°) and leftward (180°) displacements—indicated by upright red triangles (UP) and inverted blue triangles (DOWN)—suggest horizontal symmetry in the image textures. This symmetry is confirmed in Fig. 7b, where these data points lie along the $y = x$ diagonal.

The same holds for other symmetric directions; however, f_2 values for the vertical (90°) displacement are consistently higher than those for the

horizontal orientation, with slope values ranging from approximately 1.56 to 1.66. This indicates mild vertical anisotropy in texture, possibly due to weak residual gravity or temperature gradients onboard the MIR space station.

Diagonal displacements (e.g., 45°) result in even greater f_2 values, with slopes between 2.19 and 2.26. The increase in f_2 values for diagonal displacements, relative to horizontal or vertical displacements, could be explained by differences in displacement vector magnitude. Indeed, the horizontal and vertical displacements have a magnitude of $|d| = 1$ pixel, while diagonal displacements have a magnitude of $|d| = \sqrt{2} \approx 1.414$ pixels. The steeper slope observed for diagonals likely reflects this geometric factor, suggesting the following scaling law:

$$f_2 \propto |d|. \tag{11}$$

Interestingly, the slope for the 45° orientation is slightly smaller in the DOWN dataset than in the UP dataset, consistent with similar findings for f_1 (see Fig. 3b).

Using horizontal displacement as the reference, Fig. 7a shows a wide spread in f_2 values. To assess how image quantization affects f_2, we recomputed the feature at various bit depths (Fig. 8). The results show that f_2 increases nonlinearly with increasing bit depth.

This trend can be understood by considering Fig. 5. Increasing the bit depth from 1-bit to 2-bit quadruples the number of GLCM entries (from $2^1 \times 2^1$ to $2^2 \times 2^2$), allowing for more pixel pairs with larger $|i-j|$ values and thus boosting f_2.

For example, in the 1-bit image from Fig. 5b, $f_2 = 0^2 \cdot \frac{2}{12} + 1^2 \cdot \frac{10}{12} = 0.83$, based on two diagonal and ten off-diagonal GLCM entries (Fig. 5d).

For the 2-bit image (Fig. 5a), $f_2 = 0^2 \cdot \frac{1}{12} + 1^2 \cdot \frac{4}{12} + 2^2 \cdot \frac{4}{12} + 3^2 \cdot \frac{3}{12} = 3.92$, using the GLCM entries in Fig. 5c. This increase arises from the squared weighting of larger $|i-j|$ differences.

Although the precise scaling behavior is complex, the squared term k^2 in the definition of f_2, along with the observed nonlinear growth in Fig. 8, supports the approximate relationship:

$$f_2 \propto N_g. \tag{12}$$

Figure 9 confirms that f_2 values for the UP dataset (a1–a3) are shifted toward higher values compared to the DOWN dataset (b1–b3), with minimal histogram overlap. This is consistent with stronger light scattering and

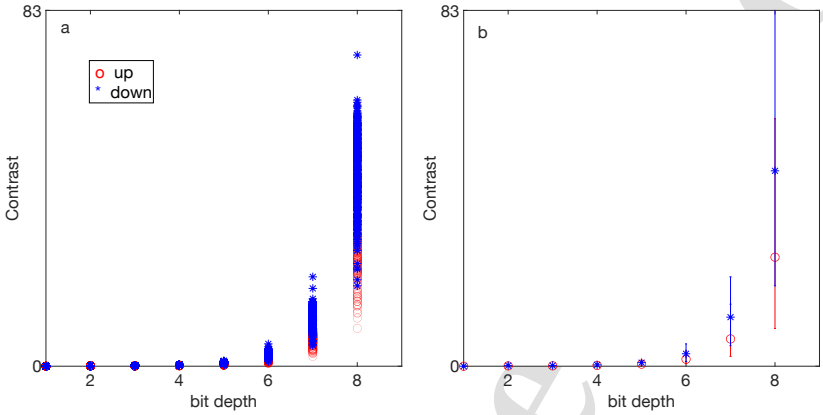

Figure 8: **Bit depth effect on Contrast feature f_2.** (a) f_2 values for each image above T_c (red circles) and below T_c (blue stars) show a broad distribution. (b) Mean and standard deviation values indicate that f_2 increases nonlinearly with bit depth.

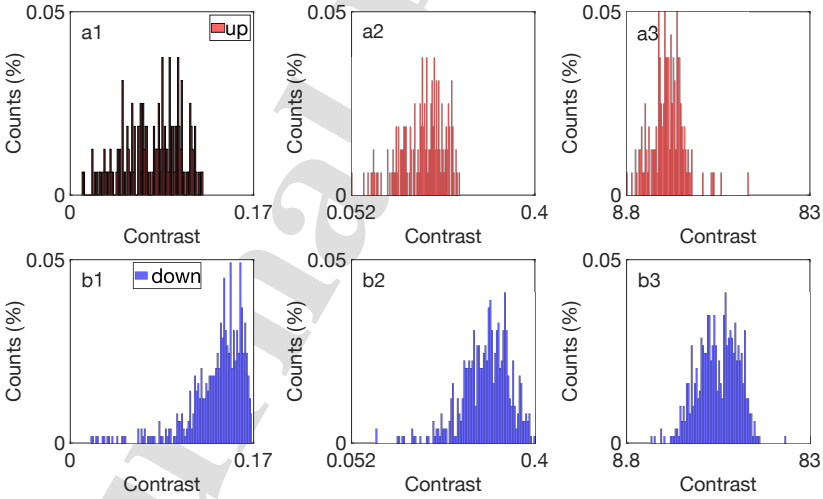

Figure 9: **Histograms of Contrast feature f_2.** Panels a1–a3 show histograms of f_2 for the UP dataset at 2-bit, 4-bit, and 8-bit depths, respectively. Panels b1–b3 show the corresponding histograms for the DOWN dataset.

enhanced fluctuations above T_c, as well as with the presence of sharp domain boundaries below T_c.

The narrower f_2 distributions observed below T_c reflect reduced fluctuation amplitudes and the emergence of ordered domains. However, the growth of liquid–vapor interfaces enhances optical contrast, contributing to the elevated f_2 values during the early stages of phase separation.

3.3. Correlation Feature f_3

Haralick defined the correlation feature f_3 as "a measure of gray-tone linear dependencies in the image" [1]. This feature quantifies how strongly the intensity of a given pixel is linearly related to that of its neighbors across the entire image [72].

As shown in Fig. 10a, f_3 values are consistently higher above T_c (mean 0.964 ± 0.007, red circles) than below T_c (mean 0.934 ± 0.009, blue stars). This indicates that f_3 is sensitive to spatial correlations in pixel intensity, particularly those arising from density fluctuations and strong light scattering above T_c. Below T_c, the onset of phase separation appears to reduce fluctuation amplitude and correlation length, disrupt the symmetry of the GLCM, and thereby lower f_3.

In addition to the horizontal displacement of $d = (1, 0)$ pixels analyzed in panel (a), Fig. 10b shows f_3 values for orientations at 45° ($d = (1, 1)$ pixels), 90° ($d = (0, -1)$ pixels), and 180° ($d = (-1, 0)$ pixels). As with f_1 and f_2, the leftward (180°) and rightward (0°) displacements yield identical f_3 values, confirming horizontal symmetry—evident from the alignment along the $y = x$ diagonal.

This symmetry also approximately holds for vertically symmetric displacements (e.g., 90° and 270°). However, the 90° orientation produces lower f_3 values, with slopes between 1.295 and 1.518, suggesting mild anisotropy between vertical and horizontal directions.

Diagonal displacements (e.g., 45°) result in even lower f_3 values, with slopes ranging from 2.014 to 2.242 relative to the horizontal reference. While slight anisotropy could contribute, these differences are largely attributed to the magnitude of the displacement vector:

$$f_3 \propto |d|. \tag{13}$$

The correlation feature reflects how rapidly the joint gray-level distribution broadens as d increases. When these features follow a power law with

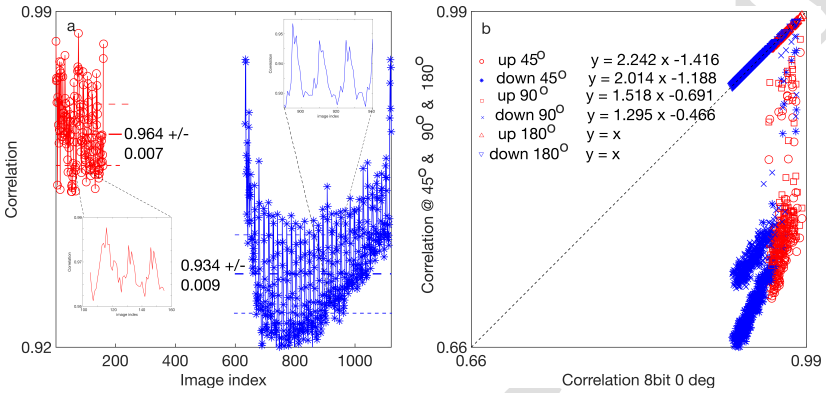

Figure 10: **Correlation feature f_3 for 8-bit depth images.** (a) f_3 values for a horizontal displacement of $d = (1, 0)$ pixels are higher above T_c (red circles), reflecting enhanced spatial correlation. Below T_c (blue stars), GLCM asymmetry due to emerging domain boundaries reduces correlation. Insets show that f_3 oscillates with a dominant frequency of approximately 1.7 Hz. (b) f_3 values for other displacement directions plotted against the horizontal reference; slopes reflect directional differences in correlation.

exponent β, the slope in log–log space quantifies the texture's "long-range" organization. Many textures in nature—e.g., cloud patterns, tissue histology, turbulent gradients—are neither purely random nor purely periodic, but exhibit statistical self-similarity over a range of scales. For such processes, second-order statistics based on the GLCM often decay as a power law with distance. From a statistical viewpoint, if the underlying field (e.g., intensity, density, or refractive index variation) has a power-law-type correlation function $C(r) \propto r^{-\gamma}$, then sums built from pairwise statistics—including some Haralick features such as Correlation—will inherit a related exponent (see Eq. 13).

We also evaluated the influence of bit depth on f_3, as shown in Fig. 11. Although the increase is less pronounced than for f_2, f_3 still rises nonlinearly with bit depth:

$$f_3 \propto N_g. \tag{14}$$

Unlike f_1 and f_2, estimating f_3 analytically is more challenging due to its dependence on the mean and standard deviation of the GLCM marginal distributions. However, we can approximate its unnormalized component

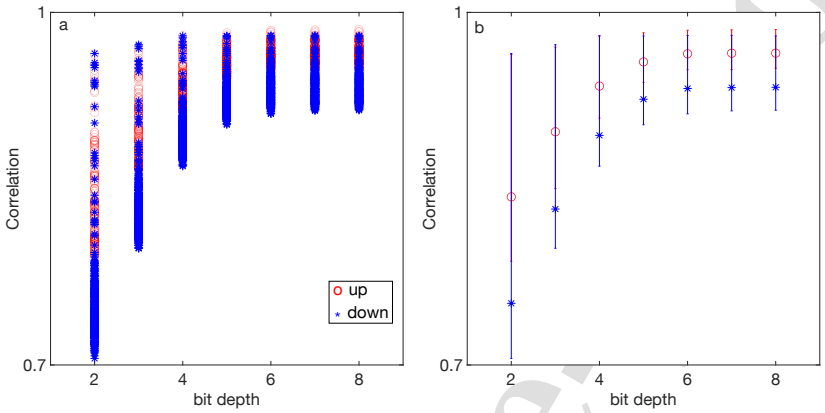

Figure 11: **Bit depth effect on Correlation feature f_3.** (a) f_3 values remain consistently high (above 0.7) across all datasets. (b) Mean and standard deviation show that f_3 increases nonlinearly with image bit depth.

using the raw correlation sum:

$$\tilde{f}_3 = \sum_{i=0}^{N_g-1} \sum_{j=0}^{N_g-1} ij\, p(i,j). \tag{15}$$

For the 1-bit image in Fig. 5b, using the GLCM in Fig. 5d and the definition from Eq. 15:

$$\tilde{f}_3 = 0 \cdot 0 \cdot \frac{1}{12} + 0 \cdot 1 \cdot \frac{5}{12} + 1 \cdot 0 \cdot \frac{5}{12} + 1 \cdot 1 \cdot \frac{1}{12} = 0.08. \tag{16}$$

For the 2-bit image in Fig. 5a, using the GLCM from Fig. 5c and the definition from Eq. 15:

$$\tilde{f}_3 = 0 \cdot 1 \cdot \frac{1}{12} + 0 \cdot 2 \cdot \frac{1}{12} + \cdots + 3 \cdot 2 \cdot \frac{2}{12} = 1.23. \tag{17}$$

As seen from Eq. 17, higher bit depth enables larger gray-level values and increases the contribution of high-weight pixel pairs to the correlation sum, compared to lower bit depth (see Eq. 16).

Figure 12 shows that f_3 histograms for the UP dataset (a1–a3) are skewed toward higher values compared to those for the DOWN dataset (b1–b3), with

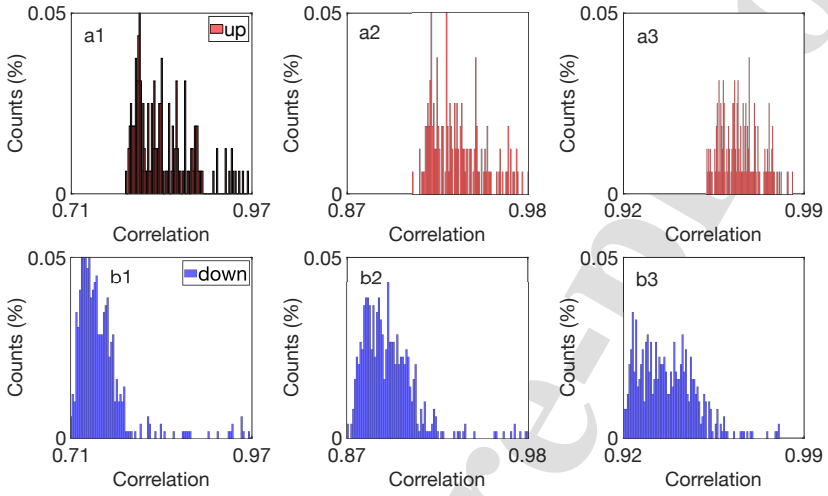

Figure 12: **Histograms of Correlation feature f_3.** Panels a1–a3 show histograms of f_3 for images above T_c at 2-bit, 4-bit, and 8-bit depths, respectively. Panels b1–b3 show the corresponding distributions for images below T_c.

minimal overlap between the two sets. This confirms that spatial correlations in pixel intensity are stronger above T_c, consistent with larger fluctuation amplitudes and longer correlation lengths near the critical point.

4. Discussion and Concluding Remarks

Despite being introduced over five decades ago [1], Haralick features remain analytically underexplored. Among the few studies that have attempted to optimize their computation—particularly with respect to the number of gray levels and other GLCM parameters—Churchill et al. [73] proposed the concept of an optimal bin width for constructing the bivariate GLCM. However, their suggested bin width of 10 corresponds to a very low image bit depth of approximately $\log_2(10) \approx 3$ bits, which is significantly lower than the 8-bit or higher bit depth quantization schemes typically used in practical imaging applications. Moreover, while Churchill et al. attempted to normalize features using the square of the bin width, they found that the features scale with different orders of complexity relative to the number of gray levels—necessitating further empirical adjustments to achieve effective

normalization.

Efforts to improve radiomics continue, particularly in standardizing imaging protocols [74, 75] and enhancing the performance of texture-based classifiers in biomedical applications [76]. A persistent challenge is the lack of a unified normalization framework for Haralick features [76, 77], which limits reproducibility and hampers the identification of robust radiomic biomarkers. Other ongoing concerns include the reproducibility of radiomic features across imaging platforms [78], the impact of convolution kernels on feature extraction [79], and the computational cost of GLCM construction for large, high-bit-depth, or multispectral images. Haralick features also exhibit sensitivity to image rotation and textural scaling [80].

Haralick features are based on the GLCM, which is computed over a sliding window with a directional displacement vector. They are local measures associated with image textures, capturing variations within small neighborhoods. This is especially useful when the texture is nonstationary—i.e., different "patches" of the image exhibit distinct statistical properties, as in the phase separation regime. It is worth noting that GLCM storage requires memory on the order of $\mathcal{O}(N_g \times N_g)$ and is independent of the image size $N_x \times N_y$. Typical GLCM bit depths are 32 or 64, although we also used 128 and 256 levels in this study. GLCM-based features can be sensitive to the quantization scheme. For example, too many gray levels can create spurious bins due to image noise and may lead to unstable features. This is why GLCMs are typically downsampled to 16, 32, or 64 gray levels. Due to their discrete nature, Haralick features can be more robust to certain types of quantization—since they summarize counts rather than amplitudes—if the quantization scheme is chosen judiciously.

Haralick features are also easy to interpret. For example, the Energy measure assesses the uniformity of the co-occurrence distribution; Contrast measures the intensity difference between neighboring pixels; and Correlation indicates how correlated a pixel is with its neighbor at offset d. For small images of 176×240 pixels, as in this study, Haralick's GLCM can still extract local gray-level pair statistics, whereas other methods—such as the Fourier Transform (FT)—may yield a spectrum that is too coarse (i.e., with low frequency resolution).

Other measures of image texture can use, for example, two-dimensional Fourier Transforms (FT). In general, the FT is a global descriptor of an image's frequency content. It cannot distinguish between texture changes in different subregions unless the image is explicitly partitioned for use with

the short-time "windowed" FT. A cropped or windowed image produces boundary-induced spectral artifacts that require additional windowing—such as the Hamming or Hann window—before applying the Fourier transform. Generally, the FT works well if the texture is homogeneous throughout the entire image. If spatial localization is essential, then the short-time Fourier transform (STFT) is required, which increases computational complexity. The computational complexity of a 2D FT is on the order of $\mathcal{O}(N_x N_y \log(N_x N_y))$, with standard image sizes exceeding 256×256 pixels; for high-quality images, sizes can exceed 1024×1024 pixels. A 2D FT is sensitive to additive noise, as even small-amplitude noise creates energy across all frequencies. Typically, one can apply a low-pass filter or compute band-limited spectra to reduce the influence of noise. However, noise may overlap with structural patterns in the frequency domain. Disentangling them requires careful filtering or thresholding. If the texture is stochastic, the FT may fail to distinguish it from uniform noise unless specific frequency bands are targeted.

This study first investigated whether the three most widely used Haralick features could reliably detect the phase transition in supercritical SF_6 under microgravity—an especially challenging setting. This question remains largely unexplored, as prior applications of Haralick features have primarily focused on phase transitions in polymers [16, 17] or microstructural changes in metals [11, 13]. Our analysis showed that all three features—Energy (f_1), Contrast (f_2), and Correlation (f_3)—displayed statistically significant differences above and below the critical temperature (see Fig. 3, Fig. 7, and Fig. 10, respectively). Because the dataset includes a well-characterized transition point [43, 60, 61], these results serve as a proof of concept for applying Haralick features to study liquid–gas phase transitions using imaging data. To summarize, we found that the three features used in this study—Energy (Fig. 3), Contrast (Fig. 5), and Correlation (Fig. 7)—can distinguish between datasets recorded above T_c (the UP dataset) and those recorded below T_c (the DOWN dataset), as shown in Table 1. The values given in Table 1 correspond to 8-bit depth images and a horizontal displacement vector of $d = (1, 0)$ pixels. They represent the mean $\pm$ standard deviation of the corresponding features.

The original dataset consists of 176×240 pixel images at a spatial resolution of approximately 3 µm per pixel (see [61] for optical details). Analysis revealed slight anisotropy under 90° rotations for all three features, possibly due to residual gravity aboard the MIR Space Station and/or weak thermal gradients. A stronger anisotropy was observed when comparing the horizon-

Table 1: Haralick Features Below vs. Above T_c

Feature	Above T_c	Below T_c
Energy (f_1)	0.037 ± 0.015	0.017 ± 0.003
Contrast (f_2)	24.6 ± 5.2	46.4 ± 7.3
Correlation (f_3)	0.964 ± 0.007	0.934 ± 0.009

tal reference displacement vector to the 45° diagonal orientation (see Fig. 3b, Fig. 7b, and Fig. 10b). This anisotropy is largely attributable to the increased magnitude of the displacement vector at 45°, which is $\sqrt{2}$ times that of the horizontal vector. After correcting for this effect—by dividing the slopes in the 45° orientation by $\sqrt{2}$—the adjusted values closely match those for the 90° direction. Thus, after accounting for vector magnitude, a consistent and modest directional anisotropy emerges, likely caused by microgravity perturbations or thermal convection. This correction enables the formulation of empirical scaling laws of the form $f \propto |d|^{\beta}$, given by Eq. 9 for f_1, Eq. 11 for f_2, and Eq. 13 for f_3.

We also evaluated how the selected Haralick features vary with image bit depth (see Fig. 4 for f_1, Fig. 8 for f_2, and Fig. 11b for f_3). This analysis led to an additional scaling relationship of the form $f \propto N_g^{\alpha}$, given by Eq. 10 for f_1, Eq. 12 for f_2, and Eq. 14 for f_3.

Histograms of each feature (see Fig. 6 for f_1, Fig. 9 for f_2, and Fig. 12b for f_3) further demonstrated minimal overlap between the UP (above T_c) and DOWN (below T_c) datasets. Notably, the DOWN distributions were consistently narrower, likely due to the reduced variability and structured morphology associated with early-stage phase separation.

It must be emphasized that consistent use of Haralick features requires that images be recorded under the same conditions—i.e., microscopic images from both the UP (above T_c) and DOWN (below T_c) regions, as shown in Fig. 1. Since the images recorded during the phase transition were acquired without the use of a microscope, the Haralick feature values from that interval cannot be directly compared to those obtained using microscopic imaging. Therefore, the precise temporal location of the phase transition could not be determined using the Haralick feature approach due to the gap between the UP and DOWN datasets. Nonetheless, based on the available microscopic images, it can be stated that all three Haralick features used in this study exhibit significant differences below T_c compared to those above T_c.

To summarize, our findings suggest that Haralick features are capable of

identifying phase transitions in pure fluids. Moreover, if the dataset were recorded under consistent imaging conditions throughout the entire phase transition, Haralick features might also serve to identify the precise moment of critical temperature crossing. Nonetheless, further datasets are needed to accurately estimate the scaling exponents α and β, and to explore their potential universality near critical points.

Data available statement

Data available on request from the authors.

Author contributions

AO: Conceptualization, formal analysis, funding acquisition, methodology, visualization, writing–original draft, writing–review & editing.

SAO: Formal analysis, funding acquisition, methodology, resources, software, validation, visualization, writing–review & editing.

YG: Funding acquisition, investigation, writing–review & editing.

CL: Data curation, funding acquisition, investigation, writing–review & editing.

DB: Funding acquisition, investigation, writing–review & editing.

References

[1] R. M. Haralick, K. Shanmugam, I. Dinstein, Textural features for image classification, IEEE Transactions on Systems, Man, and Cybernetics SMC-3 (6) (1973) 610–621. doi:10.1109/TSMC.1973.4309314.

[2] R. Haralick, Statistical and structural approaches to texture, Proceedings of the IEEE 67 (5) (1979) 786–804. doi:10.1109/PROC.1979.11328.

[3] C.-C. Hung, E. Song, Y. Lan, Texture Features and Image Texture Models, Springer International Publishing, Cham, 2019, Ch. 1, pp. 15–50. doi:10.1007/978-3-030-13773-1_2.
URL https://doi.org/10.1007/978-3-030-13773-1_2

[4] T. Papathomas, R. Kashi, A. Gorea, A human vision based computational model for chromatic texture segregation, IEEE Transactions on Systems, Man, and Cybernetics, Part B (Cybernetics) 27 (3) (1997) 428–440. doi:10.1109/3477.584950.

[5] A. V. Jagadeesh, J. L. Gardner, Texture-like representation of objects in human visual cortex, Proceedings of the National Academy of Sciences 119 (17) (2022) e2115302119. doi:10.1073/pnas.2115302119.

[6] T. Lofstedt, P. Brynolfsson, T. Asklund, T. Nyholm, A. Garpebring, Gray-level invariant Haralick texture features, PLOS ONE 14 (2) (2019) 1–18. doi:10.1371/journal.pone.0212110.

[7] A. Oprisan, S. A. Oprisan, Bounds for Haralick features in synthetic images with sinusoidal gradients, Frontiers in Signal Processing 3 (2023). doi:10.3389/frsip.2023.1271769.

[8] P. Brynolfsson, D. Nilsson, T. Torheim, T. Asklund, C. Thellenberg-Karlsson, J. Trygg, T. Nyholm, A. Garpebring, Haralick texture features from apparent diffusion coefficient (adc) mri images depend on imaging and pre-processing parameters, Scientific Reports 7 (2017) 4041. doi:10.1038/s41598-017-04151-4.

[9] J. D. Gunton, Recent Theoretical Developments in the Kinetics of First Order Phase Transitions, Springer US, Boston, MA, 1987, Ch. 1, pp. 387–411. doi:10.1007/978-1-4684-7476-3_41.

[10] P. Papon, J. Leblond, P. Meijer, The physics of phase transitions: Concepts and applications, Springer Berlin, Heidelberg, 2006. doi:10.1007/3-540-33390-8.

[11] D. L. Naik, H. U. Sajid, R. Kiran, Texture-based metallurgical phase identification in structural steels: A supervised machine learning approach, Metals 9 (5) (2019). doi:10.3390/met9050546.

[12] A. Fuchs, Application of microstructural texture parameters to diffusional and displacive transformation products, Ph.D. thesis, University of Birmingham (05 2005). doi:10.13140/RG.2.2.13094.11845.

[13] X. Liu, Microstructural characterization of pearlitic and complex phase steels using image analysis methods, Ph.D. thesis, University of Birmingham (2014).

[14] S. Dutta, K. Barat, A. Das, S. K. Das, A. Shukla, H. Roy, Characterization of micrographs and fractographs of cu-strengthened hsla

steel using image texture analysis, Measurement 47 (2014) 130–144. doi:10.1016/j.measurement.2013.08.030.

[15] S. Pieprzyk, T. Yevchenko, D. Dardas, A. C. Branka, Phase transitions and physical properties by a color texture analysis: Results for liquid crystals, Journal of Molecular Liquids 362 (2022) 119699. doi:10.1016/j.molliq.2022.119699.

[16] S. Sastry, K. Mallika, G. Bankapalli, H. Tiong, S. Lakshminarayana, Identification of phase transition temperatures by statistical image analysis, Liquid Crystals - LIQ CRYST 39 (2012) 1–6. doi:10.1080/02678292.2012.672661.

[17] L. Xu, Y. Dara, S. Magar, A. Badughaish, F. Xiao, Morphological and rheological investigation of emulsified asphalt/polymer composite based on gray-level co-occurrence matrix, International Journal of Transportation Science and Technology 14 (2024) 258–275. doi:10.1016/j.ijtst.2023.05.004.

[18] D. Beysens, J. Straub, D. Turner, Phase Transitions and Near-Critical Phenomena, Space, A European Perspective, Springer, Berlin, Heidelberg, 1987, Ch. 1, pp. 221–256. doi:10.1007/978-3-642-46613-7_7.

[19] D. Beysens, Y. Garrabos, The phase transition of gas and liquids, Physica A 281 (2000) 361–380.

[20] M. Levy, J.-C. Le Guillou, J. Zinn-Justin, Phase Transitions, Plenum, New York, 1982.

[21] A. Onuki, Phase transition dynamics, Cambridge University Press, Cambridge, UK, 2002.

[22] D. Beysens, Critical Phenomena, Materials Sciences in Space, a Contribution to the Scientific Basis of Space Processing, Springer, Berlin, Heidelberg, 1986, Ch. 1, pp. 191–224. doi:10.1007/978-3-642-82761-7_9.

[23] D. Beysens, P. Guenoun, F. Perrot, Phase separation of critical binary fluids under microgravity: Comparison with matched-density conditions, Physical Review A 38 (8) (1988) 4173–4185.

[24] D. Beysens, P. Guenoun, F. Perrot, Direct observation of critical fluctuations, Journal of Physics: Condensed Matter 2 (1990) SA127–SA133.

[25] D. Beysens, P. Guenoun, P. Sibille, A. Kumar, Dimple and nose coalescences in phase-separation processes, Physical Review E 50 (2) (1994) 1299–1302.

[26] D. Beysens, Kinetics and morphology of phase separation in fluids: The role of droplet coalescence, Physica A 239 (1997) 329–339.

[27] D. Cannell, Measurement of the long-range correlation length of sf6 very near the critical point, Physical Review A 12 (1) (1975) 225–231. doi:10.1103/PhysRevA.12.225.

[28] C. Lecoutre, R. Guillaument, S. Marre, Y. Garrabos, D. Beysens, I. Hahn, Weightless experiments to probe universality of fluid critical behavior, Phys. Rev. E. 91 (6) (2015) 06010. doi:10.1103/PhysRevE.91.060101.

[29] D. Beysens, Y. Garrabos, Near-critical fluids under microgravity: status of the ESEME program and perspectives for the ISS, Acta Astronautica 48 (5-12) (2001) 629–638. doi:10.1016/S0094-5765(01)00032-7.

[30] D. Beysens, G. Pichavant, D. Chatain, V. Nikolayev, C. Lecoutre, Y. Garrabos, Non Marangoni motion of bubble under temperature gradient, 62nd International Astronautical Congress (2010) 1–12.

[31] D. Beysens, A review on transport phenomena near the critical point of fluids under weightlessness, Frontiers in Space Technologies 3 (2022). doi:10.3389/frspt.2022.876642.

[32] E. Chimowitz, Introduction to Critical Phenomena in Fluids, Oxford University Press, Oxford,UK, 2005. doi:10.1093/oso/9780195119305.001.0001.

[33] Y. Garrabos, B. Le Neindre, P. Guenoun, B. Khalil, D. Beysens, Observation of Spinodal Decomposition in a Hypercompressible Fluid under Reduced Gravity, Europhysics Letters 19 (6) (1992) 491.

[34] Y. Garrabos, M. Bonetti, D. Beysens, F. Perrot, T. Frolhlich, P. Carles, B. Zappoli, Relaxation of a supercritical fluid after a heat pulse in the

absence of gravity effects: Theory and experiments, Physical Review E 57 (5) (1998) 5665.

[35] Y. Garrabos, C. Lecoutre, D. Beysens, V. Nikolayev, S. Barde, G. Pont, B. Zappoli, Transparent heater for study of the boiling crisis near the vapor-liquid critical point, Acta Astronautica 66 (2010) 760–768. doi:10.1016/j.actaastro.2009.08.018.

[36] P. Guenoun, F. Perrot, D. Beysens, Microscopic observation of order-parameter fluctuations in critical binary fluids: Morphology, self-similarity, and fractal dimension, Physical Review Letters 63 (11) (1989) 1152.

[37] P. Guenoun, B. Khalil, D. Beysens, Y. Garrabos, F. Kammoun, B. Le Neindre, B. Zappoli, Thermal cycle around the critical point of carbon dioxide under reduced gravity, Physical Review E 47 (3) (1993) 1531–1540. doi:10.1103/PhysRevE.47.1531.

[38] J. Hegseth, V. Nikolayev, D. Beysens, Y. Garrabos, C. Chabot, Growth and morphology of phase separating supercritical fluids (gmsf), boiling in subcritical fluids, and critical fluctuations, in: Proceedings of the Fourth Microgravity Fluid Physics and Transport Phenomena Conference, Vol. NASA/CP-1999-208526/SUPPL1, National Center for Microgravity Research on Fluids and Combustion, Cleveland, OH, 1998, pp. 184–189.

[39] J. Hegseth, A. Oprisan, Y. Garrabos, V. Nikolayev, C. Lecoutre-Chabot, D. Beysens, Wetting film dynamics during evaporation under weightlessness in a near-critical fluid, Physical Review E 72 (3) (2005) 031602. doi:10.1103/PhysRevE.72.031602.

[40] J. Hegseth, A. Oprisan, Y. Garrabos, C. Lecoutre-Chabot, V. S. Nikolayev, D. Beysens, Near-critical fluid boiling: Overheating and wetting films, European Physics Journal E Soft Matter 26 (4) (2008) 345–53. doi:0.1140/epje/i2007-10333-x.

[41] J. Hegseth, A. Oprisan, D. N. Beysens, Y. Garrabos, Imaging critical fluctuations of pure fluids and binary mixtures, Physical Review E : Statistical, Nonlinear, and Soft Matter Physics 90 (2) (2014) 022127 (8 p.). doi:10.1103/PhysRevE.90.022127.

[42] M. Moldover, J. Sengers, R. Gammon, R. Hocken, Gravity effects in fluids near the gas-liquid critical point, Review of Modern Physics 51 (1) (1979) 79–99. doi:10.1103/RevModPhys.51.79.

[43] A. Oprisan, S. A. Oprisan, J. J. Hegseth, Y. Garrabos, C. Lecoutre-Chabot, D. Beysens, Universality in early-stage growth of phase-separating domains near the critical point, Physical Review E 77 (5 Pt 1) (2008) 051118.

[44] J. Sengers, R. Perkins, Transport Properties of Fluids near Critical Points, Royal Society of Chemistry Publishing, Cambridge, UK, 2014.

[45] H. E. Stanley, Introduction to Phase Transitions and Critical Phenomena, New York: Oxford University Press, 1987.

[46] B. Zappoli, B. Daniel, Y. Garrabos, Heat Transfers and Related Effects in Supercritical Fluids, Vol. 108, Springer Netherlands, 2015. doi:10.1007/978-94-017-9187-8.

[47] M. Barmatz, I. Hahn, J. A. Lipa, R. V. Duncan, Critical phenomena in microgravity: Past, present, and future, Reviews of Modern Physics 79 (1) (2007) 1–52. doi:10.1103/RevModPhys.79.1.

[48] J. Straub, L. Eicher, A. Haupt, Dynamic temperature propagation in a pure fluid near its critical point observed under microgravity during the german spacelab mission d-2, Physical Review E 51 (6) (1995) 5556. doi:10.1103/PhysRevE.51.5556.

[49] C. Domb, J. Lebowitz, J. Lebowitz, Phase Transitions and Critical Phenomena, Academic Press, San Diego, USA. London, UK, 2001.

[50] Y. Garrabos, A. Dejoan, C. Lecoutre, D. Beysens, V. Nikolayev, R. Wunenburger, Piston effect in a supercritical fluid sample cell : A phenomenological approach of the mechanisms, Journal of Physics IV France 11 (PR6) (2001) Pr6–23–Pr6–34.

[51] V. Nagpal, S. E. Guigard, Remediation of flare pit soils using supercritical fluid extraction, Journal of Environmental Engineering and Science 4 (5) (2005) 307–318.

[52] U. Nguyen, D. Evans, G. Frakman, Natural antioxidancs produced by supercririca extraction, Blackie Academic, Glascow, 1998, pp. 103–113.

[53] C. Perakis, V. Louli, E. Voutsas, K. Magoulas, Supercritical co2 extraction of dittany oil: Experiments and modeling, Journal of Supercritical Fluids 55 (2) (2010) 573–578.

[54] I. Abdulagatov, P. Skripov, Thermodynamic and transport properties of supercritical fluids. part 2: Review of transport properties, Russian Journal of Physical Chemistry B 15 (2021) 1171–1188. doi:10.1134/S1990793121070022.

[55] J. H. Lichtenbelt, A. A. H. Drinkenburg, H. A. Dijkstra, Marangoni convection and mass transfer from the liquid to the gas phase under microgravity conditions, Naturwissenschaften 73 (7) (1986) 356–359.

[56] P. Kumar, A. Pal, M. Saxena, K. Ramakumar, Supercritical fluid extraction of uranium and thorium from solid matrices, Desalination 232 (2008) 71–79.

[57] L. Martin, A. Gonzalez-Coloma, C. E. DiŒaz, A. M. Mainar, J. S. Urieta, Supercritical co2 extraction of persea indica: Effect of extraction parameters, modelling and bioactivity of its extracts, Journal of Supercritical Fluids 57 (2) (2011) 120–128.

[58] E. Reverchon, R. Adami, Nanomaterials and supercritical fluids, Journal of Supercritical Fluids 37 (2006) 1–22.

[59] A. Guyot, J. P. Brook, A. Protat, K. Turner, J. Soderholm, N. F. McCarthy, H. McGowan, Segmentation of polarimetric radar imagery using statistical texture, Atmospheric Measurement Techniques 16 (19) (2023) 4571–4588. doi:10.5194/amt-16-4571-2023.

[60] A. Oprisan, Fluctuations, Phase Separation and Wetting Films near Liquid-Gas Critical Point, Ph.D. thesis, University of New Orleans, New Orleans, LA (2006).

[61] A. Oprisan, S. Oprisan, B. Bayley, J. Hegseth, Y. Garrabos, C. Lecoutre-Chabot, D. Beysens, Dynamic structure factor of density fluctuations from direct imaging very near (both above and below) the critical point of sf6, Physical Review E 86 (2012) 061501. doi:10.1103/PhysRevE.86.061501.

[62] D. Beysens, P. Guenoun, F. Perrot, Direct observation of critical fluctuations, Journal of Physics: Condensed Matter 2 (S) (1990) SA127. doi:10.1088/0953-8984/2/S/015.

[63] V. Emelianov, A. Lednev, V. Polezhaev, A. Ivanov, G. Putin, A. Zyuzgin, D. Beysens, Y. Garrabos, Convection and heat transfer experiments in supercritical fluid under microgravity: From mir to iss, Microgravity Science and Technology 16 (1) (2005) 164–169. doi:10.1007/bf02945969.

[64] C. Lecoutre, Y. Garrabos, E. Georgin, F. Palencia, D. Beysens, Turbidity data of weightless sf6 near its liquid-gas critical point, International Journal of Thermophysics 30 (3) (2009) 810–832. doi:10.1007/s10765-009-0582-6.

[65] R. Marcout, J. Zwilling, J. Laherrere, Y. Garrabos, B. D., ALICE 2, an advanced facility for the analysis of fluids close to their critical point in microgravity, in: 45th Congress of the International Astronautical Federation, Jerusalem, Israel, International Astronautical Federation, Paris, France, 1994.

[66] DECLIC: a facility to investigate fluids and transparent materials in microgravity conditions in ISS, American Institute of Aeronautics and Astronautics, 2006.

[67] B. Zappoli, R. Kuhl, J. Robey, A. Ivanov, Cooperative research in microgravity sciences during the french manned mir missions, Acta Astronautica 53 (12) (2003) 963–970. doi:10.1016/S0094-5765(02)00273-4.

[68] S. Biswas, N. Trappeniers, J. Hoogland, Pvt properties of sulfur-hexafluoride in the gas-liquid critical region, Physica A: Statistical Mechanics and its Applications 126 (3) (1984) 384–415. doi:10.1016/0378-4371(84)90208-5.

[69] S. Biswas, C. Seldam, Determination of the coexistence curve of sulfur hexafluoride from isochoric intercepts, Fluid Phase Equilibria 47 (1) (1989) 67–75. doi:10.1016/0378-3812(89)80050-0.

[70] A. Oprisan, S. A. Oprisan, Y. Garrabos, C. Lecoutre-Chabot, D. Beysens, Density fluctuation analysis very near above and below critical point using morphological and spatiotemporal information, Eur. Phys. J. Plus 136 (2021) 523. doi:10.1140/epjp/s13360-021-01531-8.

[71] B. Tryggvason, W. Duval, R. Smith, K. Rezkallah, S. Varma, R. Redden, R. Herring, The vibration environment on the international space station: Its significance to fluid-based experiments, Acta Astronautica 48 (2) (2001) 59–70, advanced Materials Science. doi:10.1016/S0094-5765(00)00140-5.

[72] A. C. Souza, G. C. Silva, L. Caldeira, F. M. de Almeida Nogueira, M. L. L. Junior, E. P. de Aguiar, An enhanced method for the identification of ferritic morphologies in welded fusion zones based on gray-level co-occurrence matrix: A computational intelligence approach, Proceedings of the Institution of Mechanical Engineers, Part C: Journal of Mechanical Engineering Science 235 (7) (2021) 1228–1240. doi:10.1177/0954406220942268.

[73] N. W. Churchill, E. Roudaia, J. J. Chen, A. Sekuler, F. Gao, M. Masellis, B. Lam, I. Cheng, C. Heyn, S. E. Black, B. J. MacIntosh, S. J. Graham, T. A. Schweizer, Persistent fatigue in post-acute covid syndrome is associated with altered t1 mri texture in subcortical structures: a preliminary investigation, Behavioural Brain Research 469 (2024) 115045. doi:10.1016/j.bbr.2024.115045.

[74] H. Tharmaseelan, L. T. Rotkopf, I. Ayx, A. Hertel, D. Nörenberg, S. O. Schoenberg, M. F. Froelich, Evaluation of radiomics feature stability in abdominal monoenergetic photon counting ct reconstructions, Scientific Reports 12 (1) (2022) 19594. doi:10.1038/s41598-022-22877-8.

[75] Y. Xu, L. Lu, S. H. Sun, L. N. E, W. Lian, H. Yang, L. H. Schwartz, Z. H. Yang, B. Zhao, Effect of ct image acquisition parameters on diagnostic performance of radiomics in predicting malignancy of pulmonary nodules of different sizes, Eur Radiol 32 (3) (2022) 1517–1527. doi:10.1007/s00330-021-08274-1.

[76] B. W. Park, J. K. Kim, C. Heo, K. J. Park, Reliability of ct radiomic features reflecting tumour heterogeneity according to image quality and image processing parameters, Scientific Reports 10 (1) (2020) 3852. doi:10.1038/s41598-020-60868-9.

[77] K. M. Panth, R. T. Leijenaar, S. Carvalho, N. G. Lieuwes, A. Yaromina, L. Dubois, P. Lambin, Is there a causal relationship between genetic

changes and radiomics-based image features? an in vivo preclinical experiment with doxycycline inducible gadd34 tumor cells, Radiother Oncol 116 (3) (2015) 462–6. doi:10.1016/j.radonc.2015.06.013.

[78] K. Chen, L. Deng, Q. Li, L. Luo, Are computed-tomography-based hematoma radiomics features reproducible and predictive of intracerebral hemorrhage expansion? an in vitro experiment and clinical study, Br J Radiol 94 (1121) (2021) 20200724. doi:10.1259/bjr.20200724.

[79] L. He, Y. Huang, Z. Ma, C. Liang, C. Liang, Z. Liu, Effects of contrast-enhancement, reconstruction slice thickness and convolution kernel on the diagnostic performance of radiomics signature in solitary pulmonary nodule, Sci Rep 6 (2016) 34921. doi:10.1038/srep34921.

[80] I. T. Ahmed, B. T. Hammad, N. Jamil, A comparative performance analysis of malware detection algorithms based on various texture features and classifiers, IEEE Access 12 (2024) 11500–11519. doi:10.1109/ACCESS.2024.3354959.

Acknowledgments (in editable format)

AO and SAO thank the South Carolina Space Grant Consortium for partial support of this study.

DB, YG, and CL thank the CNES space agency for the support provided using the ALICE2 facility.

Identification of Liquid-Vapor Phase Transition using the Co-occurrence Matrix and Haralick Features

Ana Oprisan1, Sorinel A. Oprisan1, Yves Garrabos2, Carole Lecoutre-Chabot2, Daniel Beysens3

1Physics and Astronomy Department, College of Charleston, Charleston, USA
2University of Bordeaux, CNRS, Bordeaux INP, ICMCB, UMR 5026, Pessac, F-33600, France
3Physique et M\'ecanique des Milieux H\'et\'erog\`enes, CNRS, ESPCI, PSL Research University, Sorbonne Universit\'e, Sorbonne Paris Cit\'e, Paris 75005, France

Declaration of interests

☒ The authors declare that they have no known competing financial interests or personal relationships that could have appeared to influence the work reported in this paper.

☐ The authors declare the following financial interests/personal relationships which may be considered as potential competing interests: